Rare Metal Materials and Engineering
Volume 49, Issue 6, June 2020
Available online at www.rmme.ac.cn

Science Press

Cite this article as: Rare Metal Materials and Engineering, 2020, 49(6): 1885-1893.

ARTICLE

Creep Deformation Constitutive Model of BSTMUF601 Superalloy Using BP Neural Network Method

Wang Chunhui[1,2], Sun Zhihui[1,2], Zhao Jiaqing[3], Sun Chaoyang[1,2], Wang Wenrui[1,2], Zhang Jiaming[1,2]

[1] University of Science and Technology Beijing, Beijing 100083, China; [2] Beijing Key Laboratory of Lightweight Metal Forming, Beijing 100083, China; [3] Key Laboratory of Advanced Reactor Engineering and Safety of Ministry of Education, Tsinghua University, Beijing 100084, China

Abstract: A series of creep tests of BSTMUF601 superalloy were carried out at different loads and temperatures to investigate creep behaviors at actual service environment. The constitutive parameters of θ projection creep model were calibrated reversely by BP neural network method with back-propagation learning algorithm based on the collected stress and strain evaluated from a diameter correction method under constant load conditions. The results show that the predicted values coincide well with experimental results and the maximum relative error is 11.8% compared with 20.9% from multivariate nonlinear regression on the initial and stable creep stages. Both the apparent creep stress exponent estimated by θ model and the transmission electron microscope (TEM) images indicate the creep deformation mechanism may be dislocation climb, further indicating the BP neural network method can describe efficiently the non-linear and complex relationship of BSTMUF601 superalloy.

Key words: BSTMUF601 superalloy; creep constitutive model; stress and strain correction; BP neural network

Muffle furnace for bright annealing is one of the critical equipment in the production of stainless steel, titanium and titanium alloy, cold rolling strip of nickel base alloy[1]. However, a variety of defects, such as necking, reduction of wall thickness, weld cracking, occur on components undergoing the long-term application of high temperature (1423 K) and self-weight (18000 kg). The BSTMUF601 superalloy, as a kind of high temperature resistant nickel base superalloy, is regarded as a promising candidate for high temperature annealing of muffle tube with excellent creep resistance, fatigue resistance and oxidation resistance, as well as good fracture toughness and microstructure stability[2]. Therefore, the characterization of creep deformation behaviors of muffle tube fabricated using BSTMUF601 superalloy at elevated temperature is significant for further estimating the thermal-creep lifetime and analyzing the governing mechanism.

Most often, the engineering strain and stress may be not used favorably to represent true strain and stress because of decreasing cross section during creep deformation. There are two ideas to evaluate available values from the unsatisfactory experimental data: geometric approximation method of specimen deformation and eliminating effect of increasing stress on creep deformation. Adopting the former method, Wang compared uniaxial with nanoindentation creep of nanocrystalline nickel[3]. The load and displacement recorded during uniaxial creep were converted into true stress and true strain by assuming a constant taper angle of 3° during creep. Zhu et al proposed a linear approximation obtained by connecting the necking point to the final fracture point for the materials exhibiting necking behavior[4]. While considering the latter, Tahami et al separated the true creep strains from the total true strains by removing time independent initial elasto-plastic strains and time independent plastic straining due to the increase of stress resulting from the finite deformation of the

Received date: June 24, 2019
Foundation item: Natural Science Foundation of Beijing Municipality (3182025); Joint Foundation of National Natural Science Foundation Committee of China Academy of Engineering Physics (U1730121); National Natural Science Foundation of China (51575039); Fundamental Research Funds for the Central Universities (FRF-BD-18-003A)
Corresponding author: Sun Zhihui, Ph. D., Associate Professor, School of Mechanical Engineering, University of Science and Technology Beijing, Beijing 100083, P. R. China, Tel: 0086-10-62334845, E-mail: sunzhihui@ustb.edu.cn

specimens or reduction of their cross section[5].

The description method of creep deformation behaviors is mainly based on the experimental creep curves to establish the equation of the creep parameters. The creep constitutive models have been developed by Rabotnov (K-R)[6], Garofalo[7], Davies[8], Blackburn[9], Evans et al[10,11] and Maruyama et al[12], so as to evaluate creep property and creep rupture life.

The θ projection concept, since the parameters are related to material properties, temperature and stress, overcomes the shortcomings of some methods which cannot reflect the deformation process under actual service conditions. Lewis and Shaw employed the θ projection parametric method to estimate component design creep lifetimes and revealed dislocation climb is creep deformation mechanism of niobium-modified 9Cr-1Mo steel weldment[13]. The original model is only composed of the first strain hardening stage and the third softening recovery item without the steady-state stage. Sun et al proposed a modified θ projection method containing all three stages of creep. The modified model was proved accurate based on the comparisons between predicted results and experimental results[14]. However, Kim et al regarded constant secondary creep region as the results of strain hardening and softening equilibrium and characterized the creep deformation mechanism transition from dislocation creep to diffusion creep with the θ projection method[15].

In order to determine the parameters of above θ projection constitutive model by the experimental data, the general inverse identification method is employed by fitting variable stress and time synchronously with optimization algorithm requiring prohibitive computing time. Thus, a new approach, based on BP neural network for inverse identification of parameters of the θ projection creep constitutive equation, was proposed to implement solution of the highly nonlinear correlation between experimental variables and constitutive parameters. The artificial neural network (ANN) has been extensively used in the parameters identification of various models because of high precision solution for nonlinear model[16-19]. Azari et al predicted radial forging force by comparing artificial neural network and multiple regressions (MR) method, and the ANN exhibited more reliable predictions than the MR model[16]. Aguir et al introduced an identification approach combining finite elements, neural networks computations and genetic algorithm of an elasto-plastic behavior model to identify the Karafillis and Boyce criterion and the Voce parameters model of the stainless steel AISI 304[17]. Abbassi et al employed the artificial neural network system and the results of the tensile test to calibrate parameters of the Gurson-Tvergaard-Needleman model[18].

In this work, the creep tests of BSTMUF601 superalloy were carried out at a range of load and temperature levels. The actual stress and strain was calculated by a new correction method for experimental records considering uniform deformation and necking. The BP neural network was employed to calibrate parameters of the θ projection creep constitutive equation, which provide a basis to evaluate creep deformation mechanism associated with TEM images.

1 Experiment

The BSTMUF601 is Ni-Cr-Al solid solution nickel-based superalloy. Chemical composition (wt%) of the BSTMUF601 superalloy is as follows: Ni: 58~63, Cr: 21~25, Al: 1~1.7, C: 1~1.8, Mn: ≤0.1, Ti: ≤0.2, and the balance is Fe. The addition of a large amount of Cr increases the oxidation resistance and corrosion resistance of the superalloy, while the addition of Al and Ti also improves strength and creep properties at elevated temperature[2,14].

The creep tests were conducted at various load levels of 974, 1131 and 1288 N under 1253 K; 448, 526 and 605 N under 1368 K with RD-100 creep test machine. The creep test temperature was set to 1253 and 1368 K approximately based on the actual service temperature of bright annealing line[20]. The selected stress range was also sufficient to cover the really stress used in industry. In order to study the creep deformation under different temperature and stress in a short period, the accelerated short-term creep tests were adopted to estimate long-term creep data. Fig.1 shows the temperature profile and testing procedure of the creep test. Resistance heating causes the inhomogeneity of temperature rise and distribution of sample[21]; therefore, the sample was heated slowly from room temperature to predetermined temperature within about 1 h and then soaked for about 3 h in the heating furnace. Most specimens underwent the initial state and steady state while the rest were continued to rupture for dwell times up to 400 h. Finally, these specimens maintained the load and were cooled to the room temperature by the natural cooling.

2 Correction of Strain and Stress

It is well known that the actual stress is difficult to be represented by the initial test stress at constant load during the creep tensile process. That is, the instantaneous true stress elevates with the decrease of the cross-sectional area of specimen. Likewise, engineering definition of strain is no longer applicable when deformation becomes considerable. Therefore, thermal-creep deformation behaviors may be unable

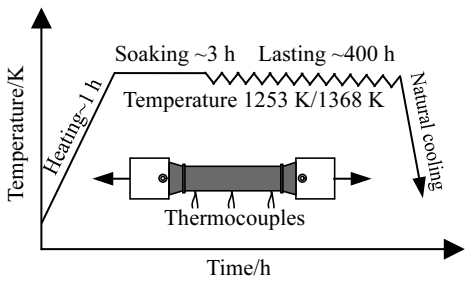

Fig.1 Temperature profile and testing procedure of the creep

to be characterized synchronously at variable stress and time[15,22]. What is more, the steady creep rate, as an important factor to evaluate creep properties of superalloy, is difficult to estimate because of the function of applied stress based on the Norton's law[23]. However, there is little attention paid to the correction of strain and stress at the creep deformation process.

In order to deal with the above issues, one direct method, constant stress creep test device[24], was introduced to obtain creep data at constant stress. And then these data was fitted by creep constitutive, such as the θ projection concept developed as a constant stress method to characterize materials creep behaviors. Whereas, some issues, such as data drift in long time test and load adjusting at necking state, are unable to be solved as usual.

Therefore, an alternative method was proposed to correct the engineering stress and strain to improve the measurement accuracy in such a way described below. Fig.2a shows the schematic of uniaxial tension creep at constant load. The gray rectangle represents the area of standard distance length of tensile creep sample schematically. The whole process of creep test includes two main periods: uniform deformation and necking deformation. In the stage of uniform deformation, the diameter and gauge distance of standard creep stretched cylindrical specimen changed from D_0 and L_0 to D_{1i} and L_{1i}, respectively. In the stage of necking deformation, the diameter of the uniform deformation section represented by double rectangles is D_{2i}. And the minimum diameter of the necking segment represented by double yellow trapezoids is D_{2i}, obtained by averaging cross section diameters after fracture based on the error correction model, although its outline is usually curved in reality[25]. In addition, the total length of the specimen is L_{2i} during necking process. There were double grating rulers on the both sides of the samples to measure the longitudinal deformation which are averaged to calculate the longitudinal strain and cannot indicate the strain at necking stage perfectly.

In this research, the creep time, temperature, tensile true stress and longitudinal true strain are the most primary data to achieve the calibration of the parameters of the creep constitutive equation.

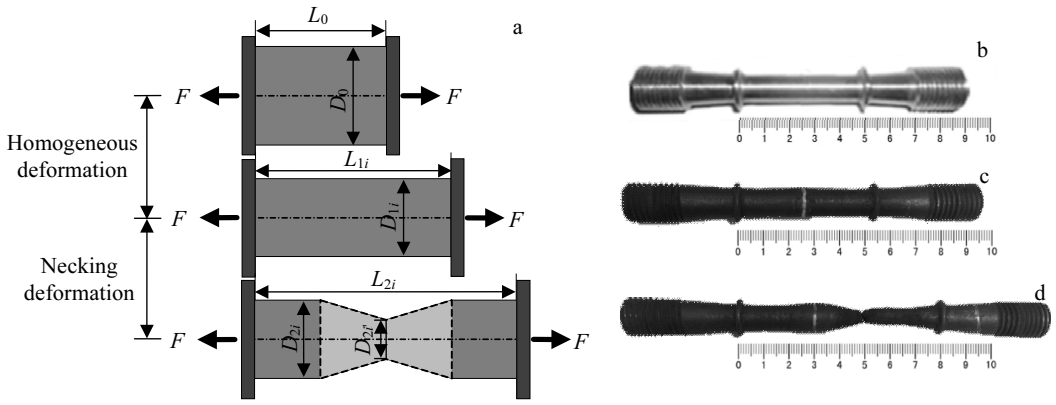

Fig.2 Schematic diagram of creep tensile process for BSTMUF601 superalloy (a) and deformation of experimental specimens at different states: (b) initial state, (c) uniform deformation state, and (d) necking state

The creep tests at 974, 1131 N (1253 K) and 448, 526 N (1368 K) are considered as uniform deformation process displayed in Fig.2c ending at the stable creep stage.

On the one hand, the longitudinal true strain ε_T is determined by[21]:

$$\varepsilon_T = \ln(1+\varepsilon_E) = \ln\left(\frac{L_{1i}}{L_0}\right) = -2\ln\left(\frac{D_{1i}}{D_0}\right) \quad (1)$$

The parameter ε_E is the longitudinal engineering strain obtained by:

$$\varepsilon_E = \frac{L_{1i}-L_0}{L_0} \quad (2)$$

The true strain was corrected by Eq.(1) at four uniform deformation conditions and compared with the true strain obtained from actual diameter of specimen after test shown in Fig.3. The relative error is introduced to evaluate quantifi-

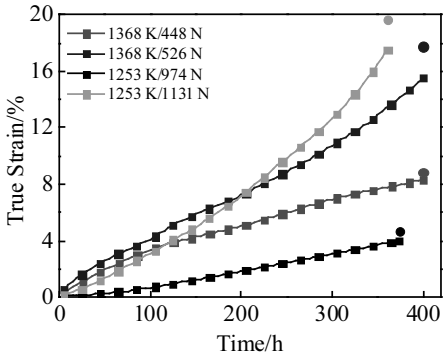

Fig.3 Comparison between corrected strain (line + symbol) and true strain (dot) obtained from actual diameter of specimen after test at temperature 1368 K, load 448 N/526 N, and temperature 1253 K, load 974 N/1131 N

cationally the accuracy of strain correction at the end of the test. And the relative error values are 5.9% at 448 N, 12.6% at 526 N, 14.9% at 974 N, 10.6% at 1131 N.

On the other hand, the true stress σ_T can be obtained by:

$$\sigma_T = \frac{4F}{\pi D_{1i}^2} \tag{3}$$

And the true diameter D_{1i}, i.e. D_T is evaluated by the longitudinal deformation from the constancy-of-volume relationship during the uniform deformation periods (Fig.2c):

$$\frac{\pi D_{1i}^2}{4} \cdot L_{1i} = \frac{\pi D_0^2}{4} \cdot L_0 \tag{4}$$

Fig.4 shows the stress curves corrected by Eq.(3) at four different uniform deformation conditions and comparison between preset stress, corrected stress and true stress. The preset stress refers to the initial stress value under the assuming condition of constant stress. The relative error values between corrected stress and true stress at the end of the test are 0.63% at 448 N, 1.99% at 526 N, 0.77% at 974 N, 1.83% at 1131 N.

Therefore, the assumption of uniform deformation is reasonable and the corresponding strain and stress correction model is available, due to the relative error of corrected strain and stress within the range of allowable experimental conditions.

Evidently, only the specimens at 605 N (1368 K) and 1288 N (1253 K) were stretched until the necking and fracture occurred among all creep conditions. During the necking periods shown in Fig.2d, it is difficult to calculate the true stress and the true strain via the above formulas because the non-uniform deformation occurred.

An approximate approach, cubic spline function is employed to interpolate the data of diameters from onset of necking to fracture, and proposed to describe these curves of creep process at necking point. Consequently, the determination of the occurrence time of necking is extremely significant to provide experimental data for the interpolating function in view of the following two assumptions: (a) Necking occurs at a point with a strain rate of 0.2 %/h, that is the starting point of accelerated creep stage at the creep test; (b) The diameter of the uniform section on the specimens remains constant from onset of necking to fracture.

The issue of occurrence time of necking is solved by tracing the strain rate based on assumption (a). The strain rate value was determined by differentiating experimental strain with respect to a time. Fig.5 shows the true strain calculated by engineering strain in Eq.(2) at uniform deformation stage and spline interpolation scheme at necking stage under 605 N/1368 K and 1288 N/1253 K.

Similarly, Fig.6 shows the true stress calculated by true diameters in Eq.(4) from the constancy-of-volume relationship at uniform deformation stage and spline interpolation scheme at necking stage under 605 N/1368 K and 1288 N/1253 K. As shown in Fig.4, the preset stress refers to the initial stress value under the assuming condition of constant stress. As can be seen from the diagram, the serious deviations between calculated fracture point and actual fracture point illustrate that the correction method of uniform deformation is not applicable to the necking period. The preset necking point based on hypothesis (a) is close to the perfect necking point based on hypothesis (b). And the actual necking point is on the left side of the perfect necking point because the diameters of the uniform section on the specimens decrease slightly with

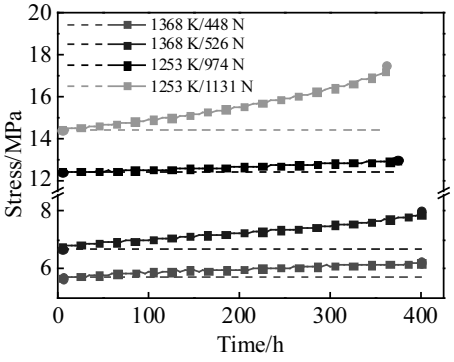

Fig.4 Comparison between preset stress (dashed), corrected stress (line+symbol) and true stress (dot) obtained from actual diameter before and after test at temperature 1368 K, load 448 N/526 N, and temperature 1253 K, load 974 N/1131 N

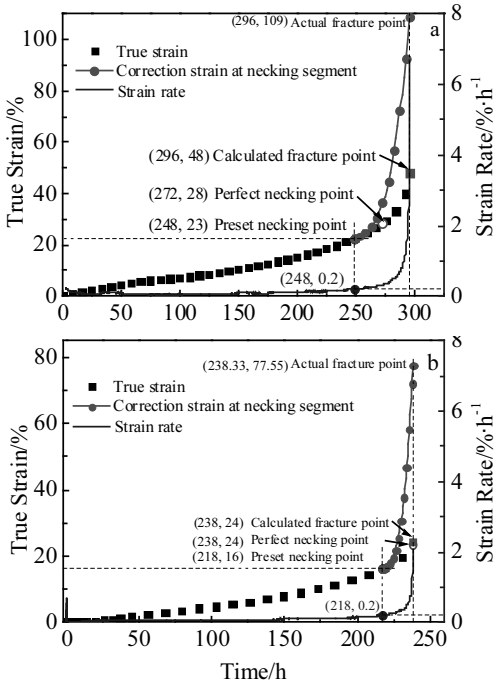

Fig.5 True strain (symbol) at uniform stage, corrected strain (line + symbol) at necking stage and strain rate (blue line) at temperature 1368 K, load 605 N (a); temperature 1253 K, load 1288 N (b)

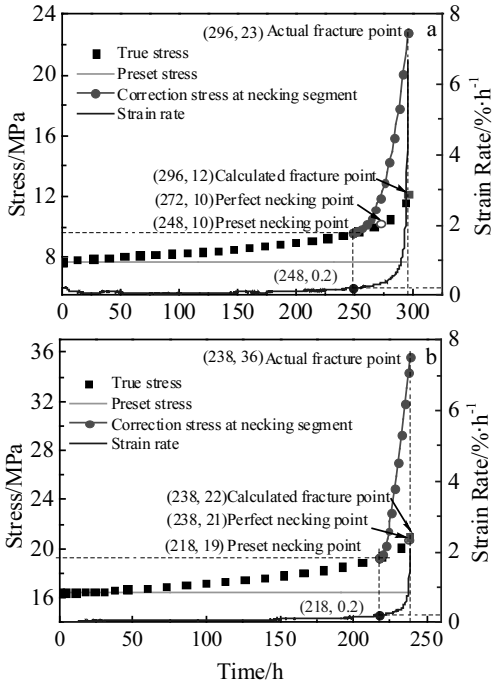

Fig.6 True stress (symbol) at uniform stage, corrected stress (line + symbol) at necking stage, preset stress (green line) and strain rate (blue line) at temperature 1368 K, load 605 N (a); temperature 1253 K, load 1288 N (b)

creep time from onset of necking to fracture. Therefore, the preset necking point is reliable to be considered as the starting point of the necking stage.

In summary, the true stress, strain at the corresponding creep time and temperature are corrected by approximate diameter estimation.

3 Calibration of Constitutive Parameters by BP Neural Network

3.1 θ projection model

Generally, high temperature creep properties of BSTMUF601 superalloy were studied by accelerated short-term creep tests and finite element simulation under reasonable stress and temperature to ensure the safety of muffle tube in actual service environment. Therefore, the effective description of creep deformation behaviors of materials requires suitable creep constitutive model with accurate parameters[17].

In order to analyze and establish a proper constitutive model for describing creep behaviors of BSTMUF601 superalloy more effectively, the θ projection method was introduced[14,26].

As a sum of the decaying stage and the tertiary accelerating stage, the constitutive equation is exhibited as follows:

$$\varepsilon = \theta_1(1-\mathrm{e}^{-\theta_2 t}) + \theta_3(\mathrm{e}^{\theta_4 t}-1) \quad (5)$$

The four θ values are determined by fitting Eq.(5) with the creep data via the least square regression analysis at constant stress and temperature[15].

In addition, each θ value is defined as a function of time and temperature so that it can be obtained from fitting for interpolation or extrapolation of the creep curves according to the following[27]:

$$\ln\theta_i = a_i + b_i\sigma + c_iT + d_i\sigma T \quad (6)$$

where σ is applied stress, T is thermodynamic temperature, and a_i, b_i, c_i and d_i (i=1, 2, 3, 4) are all independent material constants. In case if temperature is fixed, the $\ln\theta_i$ value is linear with stress and vice versa.

In a nutshell, the θ projection method establishes creep model determining the relationship between time, stress, temperature and strain by these parameters.

3.2 BP neural network model

Apparently, it is difficult to apply the experimental data of corrected stress and strain to the creep constitutive model directly, on account of the increase of true stress with creep at constant load. The BP neural network model is presented, which automatically adjusts the weight of forecast model by network training for complicated nonlinear system to realize the parameters inverse identification.

The BP neural network, as a multilayer feed-forward artificial neural network based on the error back propagation algorithm, is also applied widely, especially in high precision solution for nonlinear model[28-30].

Fig.7 shows the architecture of the three layers BP neural network for parameters identification of creep constitutive. The inputs of the neural network are composed of time,

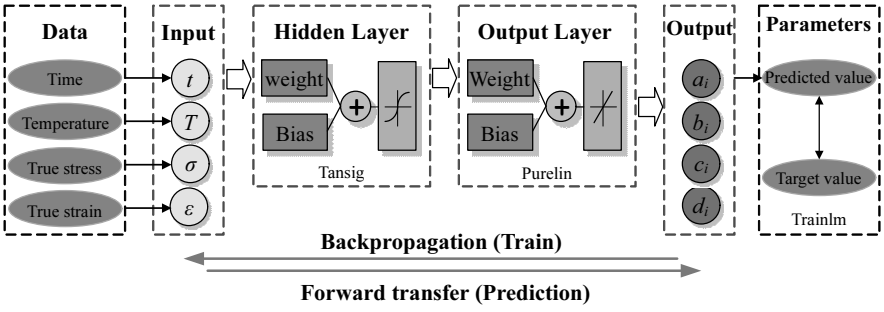

Fig.7 BP neural network model for the θ projection method

temperature, corrected stress and strain, while constitutive parameters are employed as output variables. The weight of each neuron is adjusted reversely by minimizing the training mean square error (TMSE) between the target output and the predicted output to train neural network based on the back propagation neural algorithm[18,31]. The forward transmission of the four kinds of test data predicted the corresponding constitutive parameters in trained well networks.

Classically, network topology, learning algorithm, and transfer function are the three most critical factors to determine the architecture of a neural network effecting network performance[17]. Table 1 illustrates the 4 neurons in the input layer, corresponding to the 4 variables of input time, temperature, stress and strain, and 16 neurons in the output layer, respectively, corresponding to the 16 parameters in the θ creep constitutive model. Often, the adjustment of the structural parameters of these neural networks requires repeated tests. The modeling, training and generalization of neural network were developed under MATLAB neural network toolbox.

3.3 Parameters calibration

The parameters identification procedure for creep constitutive based on BP neural network is presented in Fig.8. The whole inversion process comprises of two stages: learning and generalization. The strain values determined by the proposed parameters based on creep constitutive equation, along with other variable values are used as the training samples for the neural network at learning step. In order to cover the actual model parameters in the range of sample data as much as possible, the proposed model parameters in the training samples refer to the creep parameters of other nickel based superalloys and the initial model parameters obtained by conventional methods, although the generalization ability of neural network is excellent. In view of orthogonal design principle, the orthogonal test table with a total of 32 groups of 16 factors and 2 levels was established, in which 30 groups of samples were trained by neural network, and the remaining 2 groups of samples were tested.

Hence, the constitutive parameters exhibited in Table 2 can be identified by input of experimental data (time, temperature, corrected stress and strain) based on the trained well network previously.

Table 1 Structural parameters of BP neural network

Neural network structure	Parameters values
Neurons in the input layer	4
Number of hidden layers	1
Neurons in the hidden layer	8
Neurons in the output layer	16
Training algorithm	Levenberg-Marquardt
Activation function	Sigmoid (hidden layer) Linear (output layer)

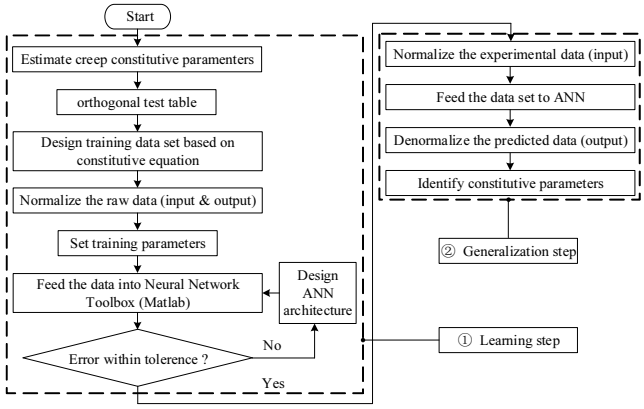

Fig.8 Logical flow chart of parameters identification

Table 2 Constitutive parameters calibrated by BP neural network

a_1 [-]	b_1 [-]	c_1 [-]	d_1 [-]
–847.968	55.178	0.618	–0.04
a_2 [-]	b_2 [-]	c_2 [-]	d_2 [-]
893.166	–62.535	–0.656	0.045
a_3 [-]	b_3 [-]	c_3 [-]	d_3 [-]
376.661	–71.542	–0.306	0.058
a_4 [-]	b_4 [-]	c_4 [-]	d_4 [-]
–410.712	70.927	0.326	–0.057

4 Results and Discussion

In order to explore the accuracy of constitutive parameters from BP neural networks, the comparisons between the experimental strain and the predicted strain were exhibited in Fig.9. The predicted strain was generated by the θ projection equation with creep parameters identified by BP model and multivariate nonlinear regression at corrected stress and temperature during the whole creep time[32]. The multivariate nonlinear regression of creep parameters were conducted by function nlinfit in MATLAB.

Fig.9 shows the evaluation of the predicted strain and the experimental strain at different test conditions, respectively. The mean relative errors between the experimental results and the predicted values using BP model are 11.8%, 3.7 %, 23.7%, 3.3%, 4.2%, 25.0% from Fig.9a~9f , respectively during the whole creep stage, while mean relative errors between the experimental results and the predicted values using nonlinear regression are 19.7%, 20.9%, 25.5%, 9.4%, 10.7%, 37.7%. These errors are in an acceptable interval indicating the BP model is competent to these conditions of steady fluctuation of stress (Fig.9a, 9b and 9d, 9e). On the other hand, the mean relative errors of Fig.9c and 9f were analyzed by dividing into two periods: before and after accelerating creep. The results before and after tertiary creep are 13.9% and 38.4% (Fig.9c); 4.0% and 61.4% (Fig.9f), respectively. It is difficult to evaluate

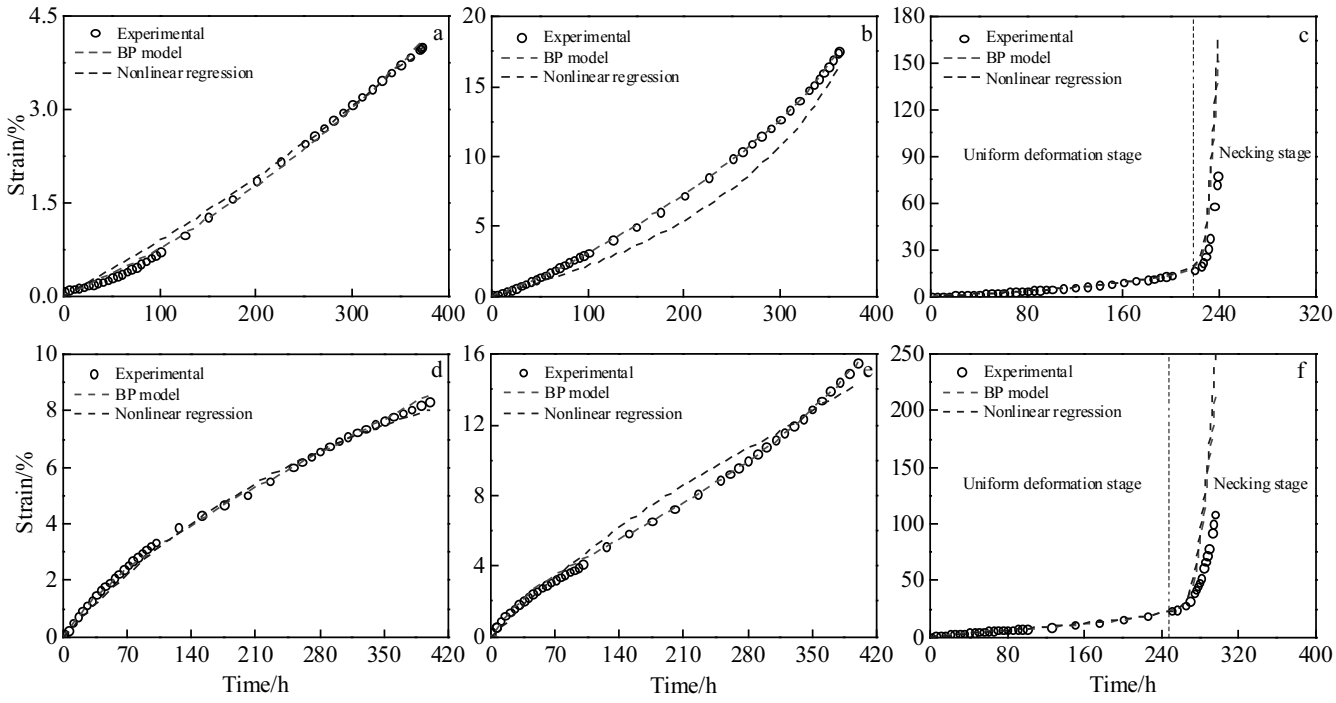

Fig.9 Comparisons between the predicted and the experimental strain at 974 N (a), 1131 N (b), 1288 N (c) under 1253 K; 448 N (d), 526 N (e), 605 N (f) under 1368 K

constitutive parameters more appropriately due to the poor projection of θ projection method at considerable stress which may be beyond the yield strength of the material at high temperature. Obviously, that proves the rationality of the BP model for the creep constitutive parameters inversion and accuracy of creep deformation prediction.

Generally, the minimum creep rate is a crucial factor to evaluate the creep property of alloy at steady-state creep stage with equilibrium between strain hardening and softening recovery. The creep rate[15] can be derived from the time derivative of the creep strain in Eq.(5) based on θ projection model characterized by BP neural network:

$$\dot{\varepsilon} = \frac{\mathrm{d}\varepsilon}{\mathrm{d}t} = \theta_1\theta_2 \mathrm{e}^{(-\theta_2 t)} + \theta_3\theta_4 \mathrm{e}^{(\theta_4 t)} \tag{7}$$

Thus, the minimum creep time which can be determined by setting the derivative of the creep rate with respect to time equal to zero and minimum creep rate are:

$$t_\mathrm{s} = \frac{1}{\theta_2 + \theta_4} \ln \frac{\theta_1 \left(\theta_2\right)^2}{\theta_3 \left(\theta_4\right)^2} \tag{8}$$

$$\dot{\varepsilon}_\mathrm{s} = \dot{\varepsilon}_{(t=t_\mathrm{s})} \tag{9}$$

In order to reveal the creep deformation mechanism of BSTMUF601 superalloy, we obtained estimates of the exponent (n) in the Norton's law:

$$\dot{\varepsilon}_\mathrm{s} = A\sigma^n \mathrm{e}^{(-\frac{Q_\mathrm{app}}{RT})} \tag{10}$$

$$n = \left(\frac{\partial \ln \dot{\varepsilon}_\mathrm{s}}{\partial \ln \sigma}\right)_\mathrm{T} \tag{11}$$

where $\dot{\varepsilon}_\mathrm{s}$ is the steady creep rate, A is material constant, n is apparent stress exponent, Q_app is apparent creep activation energy and R stands for molar gas constant (R=8.314 J·mol^{-1}K^{-1}). Of these parameters, the creep stress exponent is often considered as an useful indicator of the dominant creep mechanism, i.e. n=1 for diffusion creep such as Nabarro-Herring or Coble creep, n=2 for grain boundary sliding (GBS), and n=3~8 for dislocation creep[33].

Table 3 displays the steady-state creep rate obtained from experimental data at constant load and aforementioned θ model analysis (Eq.(9)) at constant stress. Obviously, the steady-state creep rate of the former is higher, considering the creep stress increases continuously at constant load test.

Table 3 Steady-state creep rate derived from experimental results and θ model analysis

Temperature/K	Load(N)/stress/(MPa)	Steady-state creep rate(Exp.)/%·h^{-1}[14]	Steady-state creep rate(Cal.)/%·h^{-1}
1368	448/5.7	0.00855	0.00744
	526/6.7	0.0218	0.0190
	605/7.7	0.0369	0.0287
1253	974/12.4	0.0680	0.00694
	1131/14.4	0.100	0.0149
	1288/16.4	0.250	0.0401

Therefore, the apparent stress exponent fitting between steady-state creep rate data and stress at different temperatures is shown in Fig.10. There is a linear relationship between the logarithm of the steady-state creep rate and the creep stress at same temperature. And the fitted value (n) derived from experimental results and θ model analysis are 4.9 and 4.5 under 1368 K, 4.6 and 6.2 under 1253 K, suggesting the creep deformation mechanism may be dislocation climb[13,34].

The TEM images of BSTMUF601 superalloy crept at 1368 K and 448 N (Fig.11) also support creep deformation is dislocation climb-controlled. In Fig.11a, obvious dislocations occur in alloy and pile up around γ' phase after creep tests, indicating strain hardening behavior for dislocation motion associated with obstacles in the slip plane. However, stacking

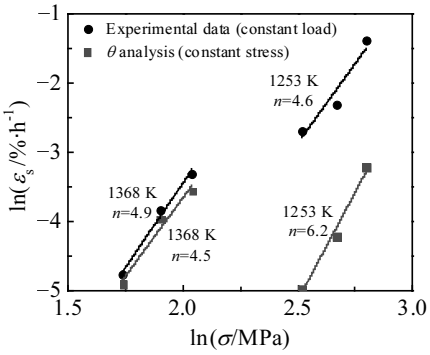

Fig.10 Creep stress exponent predicted by θ analysis

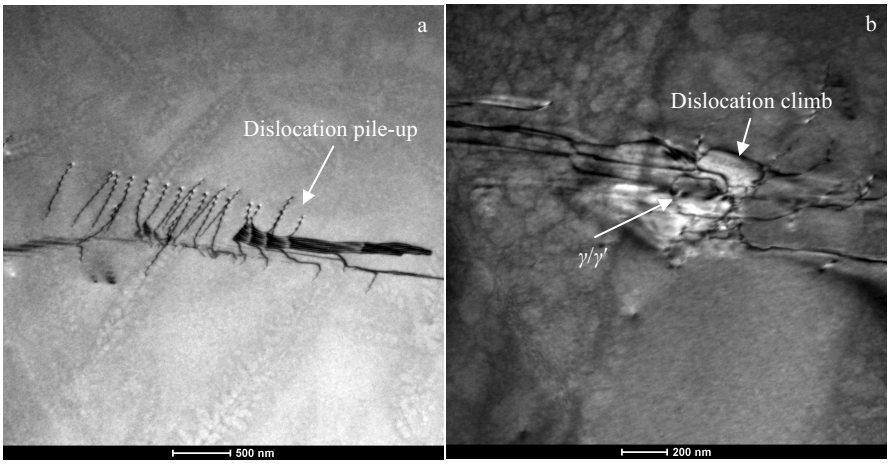

Fig.11 TEM images of BSTMUF601 superalloy after creep test at 1368 K and 448 N: (a) dislocation pile-up around γ' particles and (b) dislocation climb

faults, microtwins or Orowan loops may appear under low temperature and high stress, absent in Fig.11b when dislocation goes through the γ/γ' boundary. Climb process may have occurred, which requires diffusion and be thus time-dependent and favored by higher temperatures.

5 Conclusions

1) Due to the decrease of sectional area of specimens during creep process, the measured stress and strain deviate from their true values. Thus, the true stress and strain was corrected by approximate diameter estimation based on constant volume principle at uniform deformation stage and spline interpolation scheme at necking stage. The maximum and minimum of relative error values are 14.9% and 5.9%, respectively, at the end of the test, indicating the corrected values can more accurately represent the true stress and strain.

2) The maximum mean relative errors between the experimental results and the predicted values using BP neural network are 11.8%, compared with 20.9% from multivariate nonlinear regression on the initial and stable creep stages. The predicted results have a good agreement with the experimental strain compared with multivariate nonlinear regression, which indicates the effectiveness of the model for describing creep behaviors by the BP neural network method.

3) The apparent creep stress exponent estimated by θ analysis, experimental data and the TEM images all suggest dislocation climb may be the creep deformation mechanism.

References

1 Wang B S, Ma T J. *Baosteel Technology*[J], 2014(2): 57 (in Chinese)

2 Sun C Y, Chen G C, Wu C B *et al*. *Corrosion Science and Protection Technology*[J], 2014, 26(4): 345 (in Chinese)

3 Wang C L, Lai Y H, Huang J C *et al*. *Scripta Materialia*[J], 2010, 62(4): 175

4 Zhu S P, Huang H Z, He L P *et al*. *Engineering Fracture Mechanics*[J], 2012, 90: 89

5 Tahami F V, Daei-Sorkhabi A H, Biglari F R. *Materials Science*

and Engineering A[J], 2010, 527(18-19): 4993
6 Hu J N, Fukahori T, Igari T *et al*. *Engineering Fracture Mechanics*[J], 2018, 191: 344
7 Amalu E H, Ekere N N. *Journal of Manufacturing Systems*[J], 2016, 39: 9
8 Vanaja J, Laha K. *Metallurgical and Materials Transactions A*[J], 2015, 46(10): 4669
9 Shen J J, Ikeda K, Satoshi H *et al*. *Transactions of Nonferrous Metals Society of China*[J] 2016, 26(7): 1729
10 Mohammadi Hooyeh H, Loghman A. *Mechanics of Advanced Materials and Structures*[J], 2019, 26(11): 967
11 Xie L J, Ning D, Yang Y. *Journal of Materials Engineering and Performance*[J], 2017, 26(2): 644
12 Miyakita A, Yamashita K, Taniguchi G *et al*. *ISIJ International*[J], 2015, 55(10): 2189
13 Lewis G, Shaw K M. *Journal of Materials Engineering and Performance*[J], 2011, 20(7): 1310
14 Sun C Y, Shi B, Wu C B *et al*. *Acta Metallurgica Sinica*[J], 2015, 51(3): 349 (in Chinese)
15 Kim W G, Yin S N, Kim Y W *et al*. *Engineering Fracture Mechanics*[J], 2008, 75(17): 4985
16 Azari A, Poursina M, Poursina D. *Neural Computing and Applications*[J], 2014, 25(3): 849
17 Aguir H, BelHadjSalah H, Hambli R. *Materials & Design*[J], 2011, 32(1): 48
18 Abbassi F, Belhadj T, Mistou S *et al*. *Materials & Design*[J], 2013, 45: 605
19 Tang B, Tang B, Li J S *et al*. *Rare Metal Materials and Engineering*[J], 2013, 42(7): 1347
20 Sun C Y, Zuo X, Xiang Y *et al*. *Metals*[J] 2016, 6(3): 70
21 Sun C Y, Guo N, Fu M W *et al*. *International Journal of Mechanical Sciences*[J], 2016, 110: 108
22 Evans M. *Journal of Materials Science*[J], 2012, 47(6): 2770
23 Spigarelli S, Paoletti C. *Metals*[J], 2018, 8(1): 9
24 Nitta K, Maeda H. *Polymer Testing*[J], 2010, 29(1): 60
25 Li N, Sun C Y, Guo N *et al*. *Journal of Materials Processing Technology*[J], 2016, 228: 2
26 Sajjadi S A, Berahmand M, Rezaee-Bazzaz A. *Journal of Engineering Materials and Technology*[J], 2014, 136(1): 11 006
27 Omprakash C M, Kumar A, Srivathsa B *et al*. *Procedia Engineering*[J], 2013, 55: 756
28 Babu K K, Panneerselvam K, Sathiya P *et al*. *The International Journal of Advanced Manufacturing Technology*[J], 2018, 94(9-12): 3117
29 Singh S K, Gupta A K. *CIRP Journal of Manufacturing Science and Technology*[J], 2010, 3(1): 66
30 Sivasankaran S, Narayanasamy R, Jeyapaul R *et al*. *Materials & Design*[J], 2009, 30(8): 3193
31 Quan G Z, Lv W Q, Mao Y P *et al*. *Materials & Design*[J], 2013, 50: 51
32 Esfe M H, Afrand M, Yan W M *et al*. *International Communications in Heat and Mass Transfer*[J], 2015, 66: 246
33 Choi I C, Yoo B G, Kim Y J *et al*. *Scripta Materialia*[J], 2011, 65(4): 300
34 Wang B, Xue S B, Wang J X *et al*. *Rare Metal Materials and Engineering*[J], 2018, 47(9): 2657

基于 BP 神经网络的 BSTMUF601 高温合金蠕变本构模型

王春晖[1,2]，孙志辉[1,2]，赵加清[3]，孙朝阳[1,2]，王文瑞[1,2]，张佳明[1,2]

(1. 北京科技大学，北京 100083)

(2. 金属轻量化成形制造北京市重点实验室，北京 100083)

(3. 清华大学 先进反应堆工程与安全教育部重点实验室，北京 100084)

摘　要：通过对 BSTMUF601 高温合金在 1253 和 1368 K 不同载荷下的蠕变试验研究了马弗炉管的真实服役环境下的蠕变行为。基于一种直径修正法近似获得试件的真实应力和应变，通过误差反向传播学习算法的 BP 神经网络方法逆向标定 θ 映射法模型参数，建立恒载荷条件下的 θ 映射蠕变本构模型。结果表明，预测结果与实验结果吻合良好，蠕变初始阶段和稳定阶段的相对最大误差为 11.8%，而多元非线性回归的相对最大误差为 20.9%，模型计算的表观蠕变应力指数和 TEM 图像都表明位错攀移是蠕变变形的主导机制，说明 BP 神经网络方法对 BSTMUF601 高温合金蠕变本构模型参数识别和预测方面的优势。

关键词：BSTMUF601 高温合金；蠕变本构模型；应力应变修正；BP 神经网络

作者简介：王春晖，男，1993 年生，博士生，北京科技大学机械工程学院，北京 100083，电话：010-62332261，E-mail: b20170282@xs.ustb.edu.cn